ENGINEERING

Photopyroelectric microfluidics

Wei Li[1,2], Xin Tang[1,2]*, Liqiu Wang[1,2]*

Precision manipulation of various liquids is essential in many fields. Unlike solid objects, fluids are intrinsically divisible, enriching their fundamental operations with merging, dispensing, and splitting on top of moving. Fluids are sticky as well, calling for their lossless manipulation to prevent mass loss and contamination. We present photopyroelectric microfluidics that meet all the requirements. In response to the irradiation from even one single beam of light, our platform creates a unique wavy dielectrophoretic force field that is remarkably capable of performing desired loss-free (loss being 0.5% of existing one) manipulation of droplets of surface tension from 18.9 to 98.0 mN m^{-1} and volume from 1 nl to 1000 μl, functioning as a "magic" wetting-proof hand to navigate, fuse, pinch, and cleave fluids on demand, enabling cargo carriers with droplet wheels and upgrading the limit of maximum concentration of deliverable protein by 4000-fold.

INTRODUCTION

Manipulating buffers and organic solvents on surfaces is fundamental for many biological and/or chemical operations and thus critical in various thermal, optical, and medical applications (*1*–*9*). For any of these, it is necessary to design a platform that enables locally addressable fluids to be navigated with a low loss rate and partitioned and merged in a readily controlled manner (*10*). Light outperforms the others, mainly owing to its contactless nature, high spatial and temporal precision, and mature ray controllability promised by geometric optics, and thus culminates the most well-known optical tweezer for trapping and dislodging of micro-objects (*11*–*14*). Unlike solids, fluids span a wide spectrum of surface tensions and are intrinsically divisible, which demands an effective technique for their manipulation that could work for various fluids and perform merging, dispensing, and splitting in addition to navigating. It has been a long-standing challenge to reconcile the convenience of light and stringent demands required for liquid manipulations.

Several approaches have been exploited for photo-manipulation of liquids. They leverage the energy conversion of photoelectric, photochemical, photothermal, and photomechanical type associated with optoelectrowetting devices, light-responsive molecules, thermocapillary effect, and photodeformation of liquid crystal polymers, respectively, to materialize precise navigating and merging of fluids (*15*–*24*). However, those methods fail to split and manipulate fluids in a loss-free manner. Because of the residues, cycled washes/cleanings become necessary in processing liquids laden with different reagents, seriously increasing the time and cost involved. Moreover, most of them work only for a very narrow range of liquids and normally fail to perform for fluids with a low surface tension such as oils, alcohols, and other organic solvents because of the incompatibility between system configurations and liquid properties and the strong pinning forces caused by the preferential wetting. To date, the loss-free manipulation of such low–surface tension liquids has remained challenging because of associated issues like easy spreading and increased contact angle hysteresis.

Here, we present a previously unidentified approach by simply stacking three homogeneous layers—a photothermal film (graphene-doped polymer), a pyroelectric crystal (lithium niobate wafer), and a superomniphobic surface (silica nanosphere network)—that work in concert to enable loss-free operations of even ultralow–surface tension fluids with a single beam of light. The photothermal film is composed of graphene-polymer composite, which senses the light stimuli and responses by generating the localized and uneven thermogenesis. Consequently, the pyroelectric crystal converts the heat into extra electric charges, forming a wavy dielectrophoretic force profile that can trap, dispense, and split fluids. The superomniphobic surface interfaces fluids in a frictionless manner via maintaining an ultrastable Cassie state and preventing liquid residues. With a single beam of light serving as the stimuli, our technique can remarkably perform all four fundamental operations (movement, merging, dispensing, and splitting) of various liquids (surface tension from 18.9 to 98.0 mN m^{-1}; maneuverable fluid volume from 0.001 to 1000 μl) in a well-controlled and loss-free manner (liquid or reagent loss being only 0.5% of that associated with conventional techniques), without the need of complicated electrodes and high-voltage circuits. Our approach has, thus, great potential in substantially advancing vast fields, microassays, medical diagnosis, and droplet-enabled manufacturing and engineering, to name a few.

RESULTS

Design of photopyroelectric microfluidics

Our platform is readily fabricated by closely sandwiching a thin pyroelectric crystal (lithium niobate wafer) between a superomniphobic thin film (silica nanosphere network) and a photothermal thin film (graphene-doped polymer) (Fig. 1, A to E). For the top superomniphobic layer, we use a nanoscale fractal network fabricated via sintering hollow silica spheres covering with fluorinated surfactants for super-repellency (Fig. 1C and figs. S1 and S2) (*25*, *26*). On such surface, even silicone oil (18.9 mN m^{-1}) exhibits a contact angle θ of 151°. For the bottom layer, we homogenize the graphene nanoplatelets with polydimethylsiloxane (PDMS) and then cure the polymer to form a uniform composite film (Fig. 1E).

As a beam of near-infrared (NIR) light irradiates from the top, the translucent superomniphobic surface and pyroelectric wafer become a transparent window, allowing the NIR to readily reach the underlying composite polymer film (Fig. 1B and fig. S3). The strong photothermal effect of graphene nanoplatelets produces spatially uneven localized temperature rise. Through interfacial heat transfer,

[1]Department of Mechanical Engineering, The University of Hong Kong, Hong Kong. [2]HKU–Zhejiang Institute of Research and Innovation (HKU-ZIRI), Hangzhou, Zhejiang 311300, China.
*Corresponding author. Email: tangxin@connect.hku.hk (X.T.); lqwang@hku.hk (L.W.)

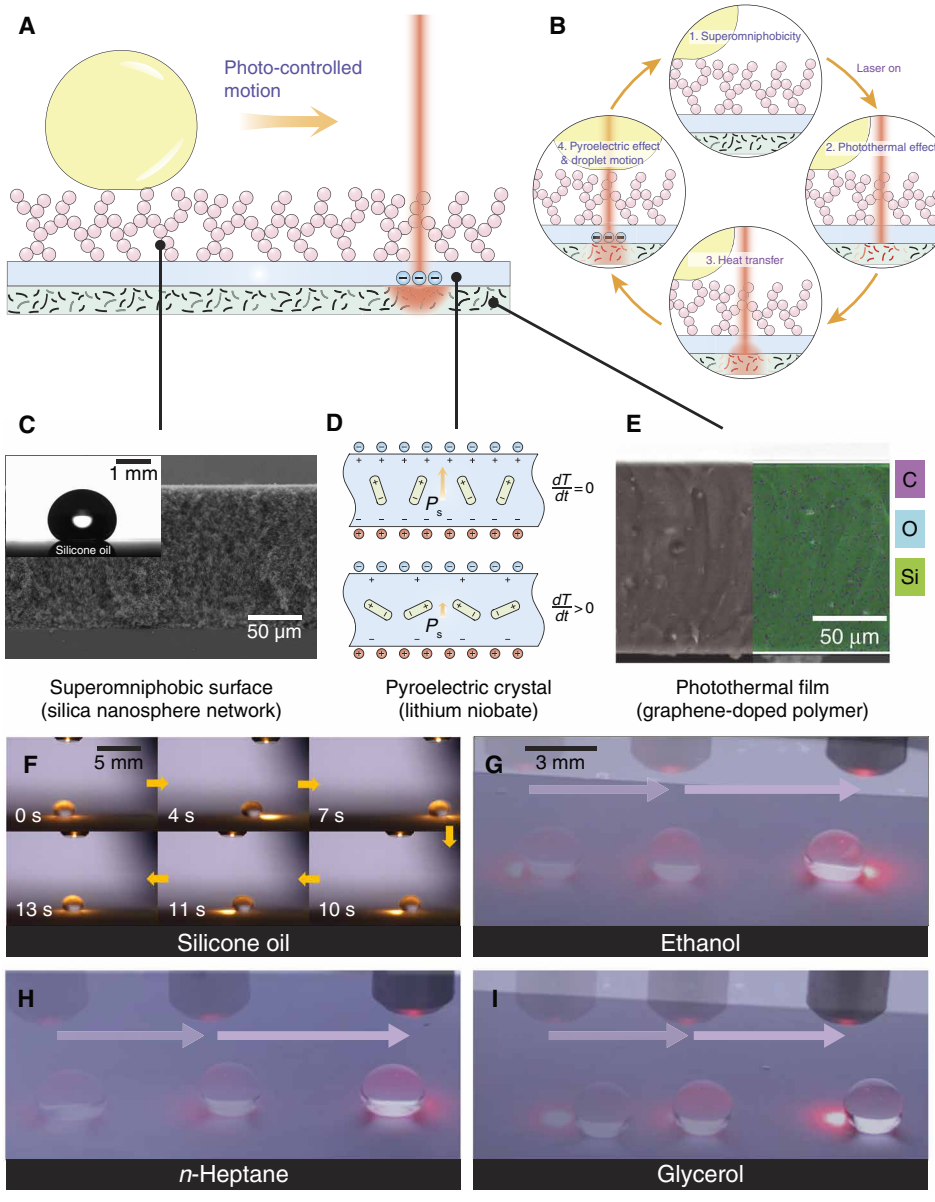

Fig. 1. Design of photopyroelectric microfluidics. (**A**) Schematic of the trilayered photopyroelectric platform consisting of the superomniphobic surface (silica nanosphere network), pyroelectric crystal (lithium niobate), and photothermal film (graphene-doped polymer) where droplets are controlled by a near-infrared (NIR) light. (**B**) Schematics showing the mechanism of photopyroelectric microfluidics. As light irradiates, the photothermal film composed of graphene nanoplatelets produces heat because of photothermal effect. Through heat transfer, the temperature within the pyroelectric crystal rises, prompting surface free charges, which drives the droplet into motion through dielectrophoretic force. (**C**) Scanning electron microscopy (SEM) cross-sectional image of the superomniphobic surface. Inset is the image of a 5-μl silicone oil residing on the surface with a contact angle of 151°. (**D**) As the temperature increases, the spontaneous polarization of pyroelectric crystal decreases, giving rise to extra surface free charges. (**E**) Cross-sectional SEM and energy-dispersive x-ray spectroscopy images of the graphene-polymer composite film, showing homogeneously dispersed graphene. (**F**) Sequential images showing a continuous manipulation of a 5-μl silicone oil using a 785-nm laser. Laser is turned on at 0 s, unless otherwise specified. (**G**) Chronophotographs showing a continuous manipulation of an ethanol droplet. (**H**) Chronophotographs showing a continuous manipulation of an *n*-heptane droplet. (**I**) Chronophotographs showing a continuous manipulation of a glycerol droplet. Photo credit: Wei Li, The University of Hong Kong.

the pyroelectric crystal is subsequently heated. As a result, the spontaneous polarization within the crystal is reduced, lowering the bound surface charges and giving rise to extra surface free charges. Droplets atop the superomniphobic surface can then be driven toward the irradiated spot by dielectrophoretic force (see note S1 for detailed design guidelines).

Our technique has proven to be effective for a wide spectrum of liquids (surface tension from 18.9 to 98.0 mN m^{-1}). As shown in Fig. 1 (F to I), the motions of different organic liquids such as silicone oil, alkanes (*n*-heptane), and alcohols (ethanol and glycerol) can be readily guided by an NIR light beam (movie S1). Such platform works as a channel-free and open-space fluidic processor, without

any electrodes or micropatterning needed in its counterpart techniques (such as digital microfluidics), which requires high-voltage circuits and multistep microfabrications in clean rooms (*27*, *28*).

Loss-free fluid interfacing and sensitive light sensing

Numerous inverted microstructures cap the fractal network of superomniphobic surfaces (Fig. 2B) and provide additional supports to suspend diverse liquids such as water, silicone oil (PDMS), ethanol, *n*-heptane, acetone, dimethylformamide (DMF), dichloromethane (DCM), and ethyl acetate in Cassie states (Fig. 2A). Fluids with surface tension spanning from 18.9 to 98.0 mN m^{-1} have large contact angle (150° to 170°) and low roll-off angle (≤5°) on the prepared superomniphobic surfaces (Fig. 2C, fig. S4, and table S1). Moreover, the surface is chemical resistant to corrosive acids and bases, including concentrated HNO_3, H_2SO_4, and KOH, and can maintain a stable Cassie state atop it, making it suitable for chemical fluidic processing.

By measuring the critical roll-off angles, we can calculate the lateral adhesive force acting on the droplet through its balance with the on-plane gravitational force $F_\gamma = mg \sin \theta_{roll-off}$, where m, g, and $\theta_{roll\text{-}off}$ denote the mass of droplet, gravitational acceleration, and roll-off angles, respectively. As shown in Fig. 2D, the lateral adhesive force is inversely proportional to the surface tension. To verify such counterintuitive negative linear correlation, we compare with those in other reported works such as in (*29*) in Fig. 2D, showing agreement with our work. Such phenomenon may originate from the fact that although the surface tension decreases, more microscopic liquid/solid contacts develop and thus yield the increased lateral adhesive force.

The mobility of fluids on the surface is further verified by liberating an *n*-heptane (20.1 mN m^{-1}) droplet from a height of ~3 cm (Fig. 2G and movie S2). After four rebounds, the *n*-heptane lastly rests on the surface. Even the ejected tiny satellite droplet can rebound on the surface as well, showing the high mobility of fluids on the surface.

Although the mobility implies ready motion, it cannot guarantee that the loss of liquid or reagent is small. To probe the liquid retention, we perform fluorescence imaging using Nile red (1.0 mg ml^{-1}) in silicone oil as the test fluid. Another two commonly used liquid-repellent surfaces, polytetrafluoroethylene (PTFE) film and slippery liquid infused porous surface (SLIPs), are used for comparisons (*30*, *31*). A test droplet is allowed to roll off or slide on the three types of surfaces tilting at an angle of 5°. As shown in Fig. 2E, obvious liquid residues are observed on the PTFE film, and its surface is contaminated by pollutants in ambient environments. Although no liquid residue is left on the SLIPs, obvious reagent traces are detected. In sharp contrast, no residue can be probed on our prepared superomniphobic surface essentially. A careful examination shows that on the superomniphobic surface, the fluorescence intensity and fraction area are only 0.6 and 0.5% of those on the PTFE surface (Fig. 2F), implying a nearly loss-free contact with the fluids.

Then, we examine the light-sensing component of the system. As a beam of 785-nm laser irradiates, the temperature peaks at the laser spot center and decays toward its surroundings as shown by the infrared thermal imaging (Fig. 2H). As light illuminates at a power of 400 mW, the temperature of 5 weight % (wt %) graphene composite film rapidly ramps to 40°C in 5 s, a level enough to drive droplets into motions (Fig. 2I). Thereby, we use a 5 wt % graphene composite film to sense the light. The impact of laser power on the thermogenesis is also examined (Fig. 2J). The temperature rise depends linearly on the power, which is consistent with the theoretical analysis using a semi-infinite body heat transfer model (see note S2 for details). Therefore, our technique converts irradiated light spot into a sharply bulged temperature profile, interacts with fluids in a frictionless and loss-free manner, and works for a wide variety of fluids.

Droplet dynamics on photopyroelectric platform

To understand the actuation mechanism of the photopyroelectric platform, we examine the motion behavior of a 5-μl water droplet initially placed at a position ~13 mm away from the light spot center (Fig. 3A). After the laser is turned on, the droplet is attracted toward the illumination in a damping oscillation manner (movie S3). The droplet initially accelerates toward the laser and rapidly brakes and reverses its direction once it reaches the light spot's edge. Such decaying oscillation lasts for four cycles, after which the droplet is trapped at the position ~2 mm away from the laser spot center, a position slightly offset from the laser spot center.

To detail the manipulation and unravel the underlying physics, we performed a numerical simulation to study the droplet dynamics (see note S3 for details). Temperature distribution in pyroelectric crystal is first simulated using a finite-element method by considering the light-triggered thermogenesis as the source term in the heat conduction equation (Fig. 3B). The surface charge density σ in the crystal varies linearly with the temperature rise as $\sigma = P_c \Delta T$, where P_c and ΔT denote the pyroelectric coefficient and change of temperature, respectively (*32*). The electric field strength E is then simulated by applying a charge density boundary condition of σ on the lithium niobate wafer surface (Fig. 3C).

The dielectrophoretic force F_E on the droplet from the nonuniform electric field can be approximated as follows (*33*)

$$F_E = 4\pi {r_0}^3 k \varepsilon_0 (E \cdot \nabla) E \quad (1)$$

where r_0 is the radius of the droplet, k is the Clausius-Mossotti factor ($k = (\varepsilon - \varepsilon_0)/(\varepsilon + 2\varepsilon_0)$), and ε_0 and ε are the permittivity of air and droplets, respectively. Equation 1 is derived under the assumption that the dipole is small compared with the scale of nonuniformities of electric field. We use it to correlate F_E, with E at the droplet mass center as the first-order approximation. In a two-dimensional configuration, we only consider the dielectrophoretic force in the r direction and neglect the field strength variation in the z direction for simplicity. The lateral dielectrophoretic force thus reads

$$F_{E,r} = 4\pi {r_0}^3 k \varepsilon_0 E_r \frac{\partial E_r}{\partial r} \quad (2)$$

where E_r is the r-component of electric field strength. Thereby, the dielectrophoretic force $F_{E,r}$ is mainly determined by the variation of $E_r \frac{\partial E_r}{\partial r}$ along the r-direction.

On the basis of the simulation results, the $E_r \frac{\partial E_r}{\partial r}$ changes rapidly and reverses its sign at the edge of the laser spot (Fig. 3D). The droplet will then experience attraction when it is far away from the laser spot, but repulsion once moved into the irradiated region and be lastly immobilized at the edge of the laser spot, the position where the potential energy is the lowest (fig. S5). We simply assume that the dielectrophoretic force acts at the droplet's center of mass, which is ~1 mm above the pyroelectric crystal surface. Therefore, the $E_r \frac{\partial E_r}{\partial r}$

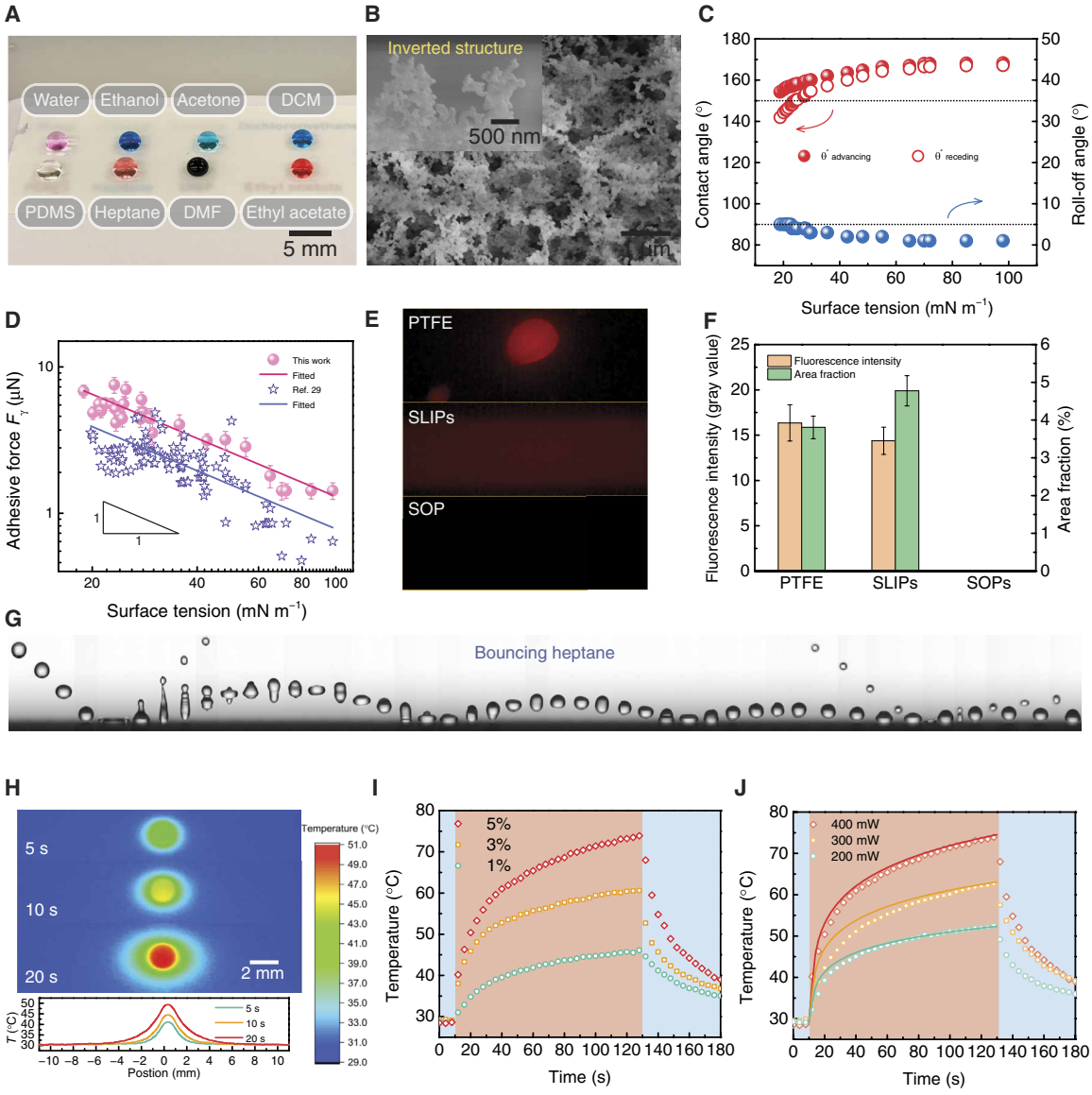

Fig. 2. Characterization of the fluid interfacing and light sensing. (**A**) Image of droplets of water, ethanol, acetone, dichloromethane (DCM), silicone oil (PDMS), *n*-heptane, dimethylformamide (DMF), and ethyl acetate residing atop the translucent superomniphobic surface. (**B**) SEM image showing the fractal network of the superomniphobic surface. Inset shows the typical inverted structures. (**C**) Super-repellency toward various liquids. (**D**) Adhesive force is inversely proportional to the surface tension. Error bars denote SD of three independent measurements. (**E**) Liquid residue detected on diverse omniphobic surfaces by fluorescence imaging. (**F**) Fluorescence intensity and area fraction of the images in (E), showing the remarkably reduced liquid loss on the superomniphobic (SOP) surface. Error bars denote SD of three independent measurements. (**G**) Sequential images showing an *n*-heptane droplet ($r_0 \approx 1$ mm, $We \approx 20$) bounces on the surface, exhibiting low adhesion toward organic liquids. Time interval between each snapshot is ~4 ms. (**H**) Infrared thermal imaging and the plot showing the temperature distribution on photothermal film upon 400-mW laser irradiation. (**I**) Thermal response of graphene-PDMS composite films with varying contents of graphene nanoplatelets to 400-mW laser irradiation. Blue and red shaded regions denote off and on states, respectively, of the 785-nm laser. (**J**) Thermal response of PDMS film containing 5 wt % graphene nanoplatelets to laser power. The solid lines are from theoretical analysis (see note S2 for details). Photo credit: Wei Li, The University of Hong Kong.

is extracted from such position to calculate the dielectrophoretic force. The general profile of $E_r \frac{\partial E_r}{\partial r}$ is similar for different extracting positions, but its magnitude increases as the position approaches the platform surface (fig. S6). The acceleration is then calculated on the basis of the numerical results using the equation as follows

$$F_{E,r} - F_\gamma = ma \quad (3)$$

Upon irradiation, the temperature gradient on the superomniphobic surface is so weak that the force caused by the thermocapillary effect is two orders of magnitude lower than the dielectrophoretic force; thereby, we neglect the thermocapillary effect here (fig. S7; see note S4 for details). To verify the simulation, we experimentally determine the acceleration of a 5-μl water droplet during the damping oscillation by recording its motion trajectory. As shown in Fig. 3E, the calculated acceleration agrees well with the measured one, confirming

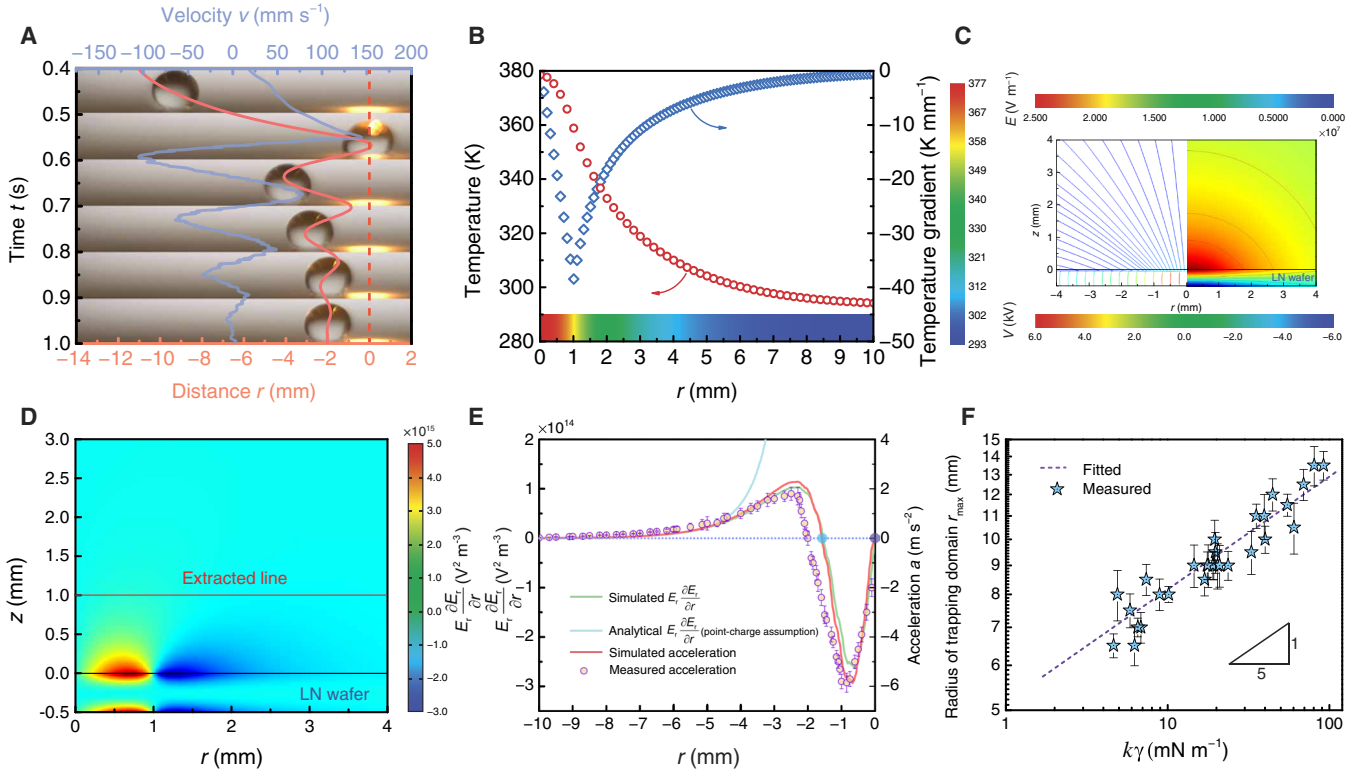

Fig. 3. Droplet dynamics on photopyroelectric platform. (**A**) Typical decaying oscillation of a 5-μl water droplet using a 400-mW NIR laser irradiation. After four oscillations, the droplet is immobilized at the edge of the laser spot. The red dashed line denotes the position of the laser spot center. Laser is turned on at ~−40 s. (**B**) Temperature mapping within the pyroelectric crystal through numerical study. (**C**) Plot of the electric field strength lines (left) and electric potential (right) obtained using the finite-element method. (**D**) Mapping of $E_r(\partial E_r/\partial r)$ surrounding the heated pyroelectric crystal. The laser beam irradiates on the region of $0 < r < 1$ mm. LN, lithium niobate. (**E**) Spatial profile of $E_r(\partial E_r/\partial r)$ and droplet acceleration. Green solid line represents the simulated $E_r(\partial E_r/\partial r)$ along the extracted line shown in (D); blue solid line represents the theoretical $E_r(\partial E_r/\partial r)$ with the point-charge assumption (see note S5); red line and orange dots represent the calculated and measured droplet accelerations, respectively; and blue and purple dots, respectively, denote the positions where dispense and split happens. The laser beam irradiates on the region of -1 mm $< r < 0$. The measured accelerations are averaged values of five frames in 5 ms, and the error bars denote the SD of the average. (**F**) The radius of fluids' trapping domain is in proportion to the product of surface tension and Clausius-Mossotti factor. Error bars denote SD of three independent measurements. The results are obtained after laser irradiates for ~40 s. Photo credit: Wei Li, The University of Hong Kong.

the wavy force profile experienced by the moving droplets. The maximum dielectrophoretic force for the tested liquids is calculated to be ~10 μN, a value large enough to overcome the lateral adhesive forces from the superomniphobic surface.

The above derivation details the variation of actuation as the droplet is proximate to the laser irradiation. When the droplet is far away from the laser spot, the analysis can be further simplified to determine the onset condition of droplet motion (see note S5 for details). With such condition, the surface charges can be approximated to be a point charge, whose field strength is described by the Coulomb's law, $(E \cdot \nabla)E \propto r^{-5}P^2$, where P denotes the laser power. As shown in Fig. 3E, the analytical $E_r\frac{\partial E_r}{\partial r}$, denoted by the blue line, agrees well with the simulated one when a droplet is more than 5 mm away from the laser spot. Thus, the dielectrophoretic force reads $F_E \propto kr^{-5}P^2$. The further away the droplets, thereby, the longer irradiation time is required to actuate it. On the onset of droplet's motion, the dielectrophoretic force balances the lateral adhesive force. As the adhesive force varies inversely with the surface tension γ, we can obtain the maximum radius r_{max} of trapping domain, the maximum initial distance from the laser spot where droplet can be actuated by a laser illumination, as $r_{max}^5 \propto k\gamma P^2$. By varying the liquid types, we confirm this relationship in Fig. 3F. Therefore, the higher relative permittivity and surface tension the liquid has, the easier the droplet can be moved.

Fluidic operations

With our photopyroelectric platform, we can perform various fluidic operations using a single beam of laser light (Fig. 4A). As shown in Fig. 4B and movie S4, the wavy dielectrophoretic force profile (similar to a distorted sine wave) can unexpectedly trap and move droplets with a volume as low as 0.001 μl, which is two orders of magnitude lower than that of its electric counterparts (such as digital microfluidics; table S2). A 200-μl liquid puddle can be losslessly handled on the platform as well. Such a broad volume range of fluids can facilitate the further miniaturization of various biomedical systems. However, there is a maximum laser-moving velocity beyond which the droplet cannot keep up with the laser movement. As shown in Fig. 4C, the faster the laser moves, the shorter time the platform is irradiated, thus leading to a lower local temperature. By increasing the laser power, such a maximum laser speed can be increased. The motion control on the platform enables the merging of droplets naturally as shown in Fig. 4D and movie S5.

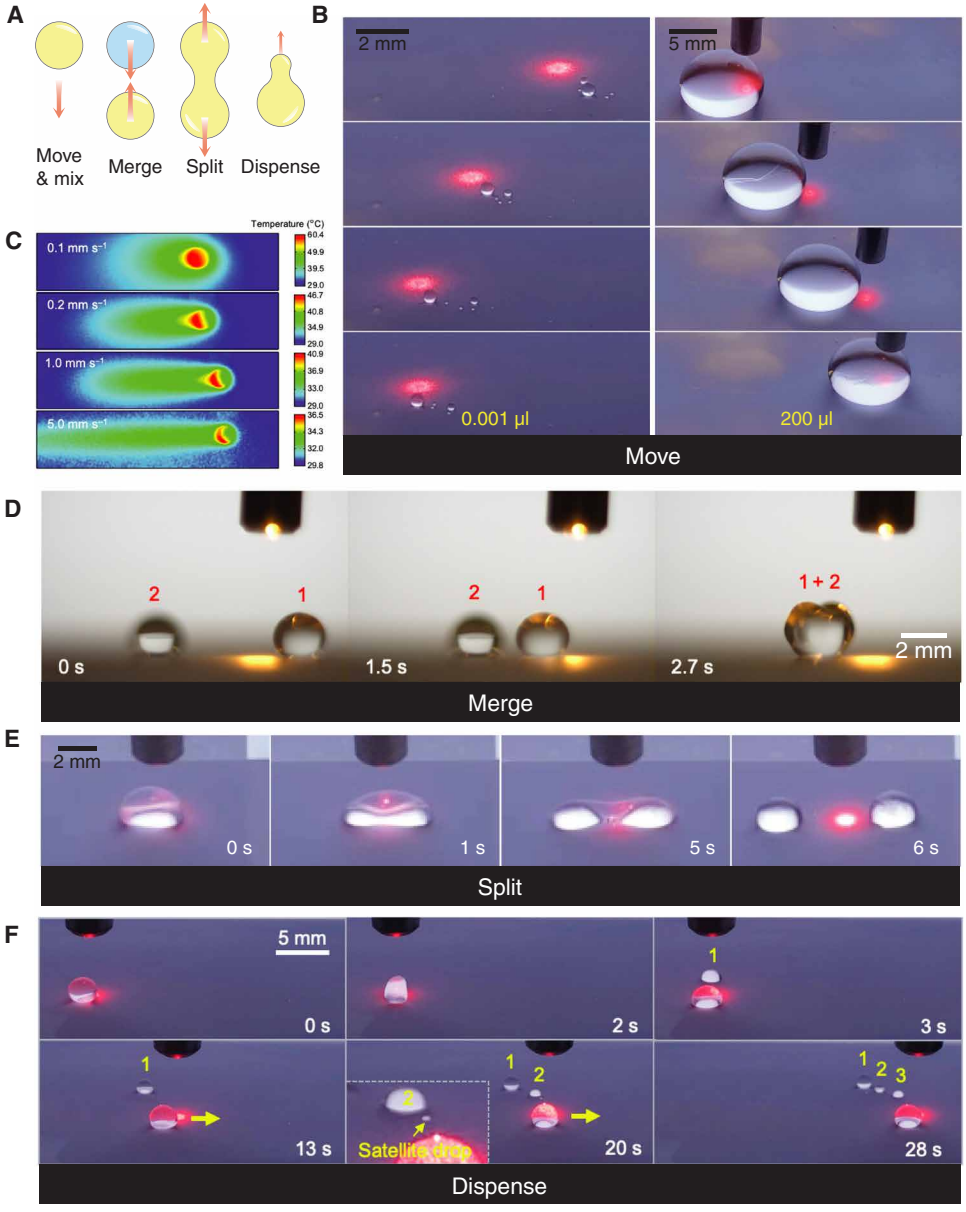

Fig. 4. Fluidic operations. (**A**) Schematics showing four fundamental fluidic operations, including navigate, merge, split, and dispense. (**B**) Guided motions of a 0.001-μl silicone oil and 200-μl water droplets, showing the broad controllable volume range. (**C**) Infrared thermal imaging showing the temperature distribution within pyroelectric crystal along the direction of moving laser spot. (**D**) Sequential images showing the merge between two isolated water droplets. (**E**) Sequential images showing the split of an ethanol droplet upon a centered prolonged irradiation. Laser is turned on at ~−2 s. (**F**) Sequential images showing the dispenses of liquid portions from a silicone oil droplet through offset prolonged irradiation. Photo credit: Wei Li, The University of Hong Kong.

The droplet can be split and even dispensed with one single beam of laser light through prolonged laser irradiations (~5 s). As shown in Fig. 4E and movie S6, the laser spot is positioned at the center of a droplet. After 5-s irradiation, the wavy dielectrophoretic force profile enables a diverging force in the opposite direction (denoted by the purple dot in Fig. 3E). The droplet is then stretched gradually, forming two separating lobes. Once the force is strong enough to overcome the surface tension, the droplet undergoes fission, giving rise to two portions apart from each other. Similarly, as shown in Fig. 4F, by simply offsetting the laser, the droplet is positioned in the local trapping spot (denoted by the blue dot in Fig. 3E). Longer irradiation creates an opposite but slightly different force pair. Such forces prompt the ejection of a smaller liquid portion from the liquid reservoir. Such light-mediated liquid split and dispense have not been reported before. Thereby, the photopyroelectric platform fully exploits the divisible nature of liquid and provides a full landscape of fluidic operation in a well-controlled manner.

Versatility and biocompatibility

Because of the extremely low friction, a droplet on the superomniphobic surfaces is normally susceptible to slight unevenness, which could lead to failure of reliable droplet control. Our platform exhibits,

however, a strong navigating force that can enable the droplet to even ascend uphill (*34*). As shown in Fig. 5A and movie S7, the droplet is elongated by the attractive force as it approaches the surface. Upon its detachment, the droplet rapidly rolls uphill at a velocity >150 mm s^{-1}. After a typical damping oscillation, the droplet is immobilized near the light spot at 0.280 s. Similarly, a second droplet is released and then ascends the slope, merging with the first one and is trapped by the light irradiation. Moreover, as the platform is placed vertically, the droplet can even ascend upward, defying the gravity (Fig. 5B and movie S8).

Our superior technique for precision manipulation of various liquids at the micro-/nanoliter scale enables the deployment of millimeter-scale cargo carriers that are of fundamental importance in many fields (*3*). As shown in Fig. 5C and movie S9, a cargo carrier

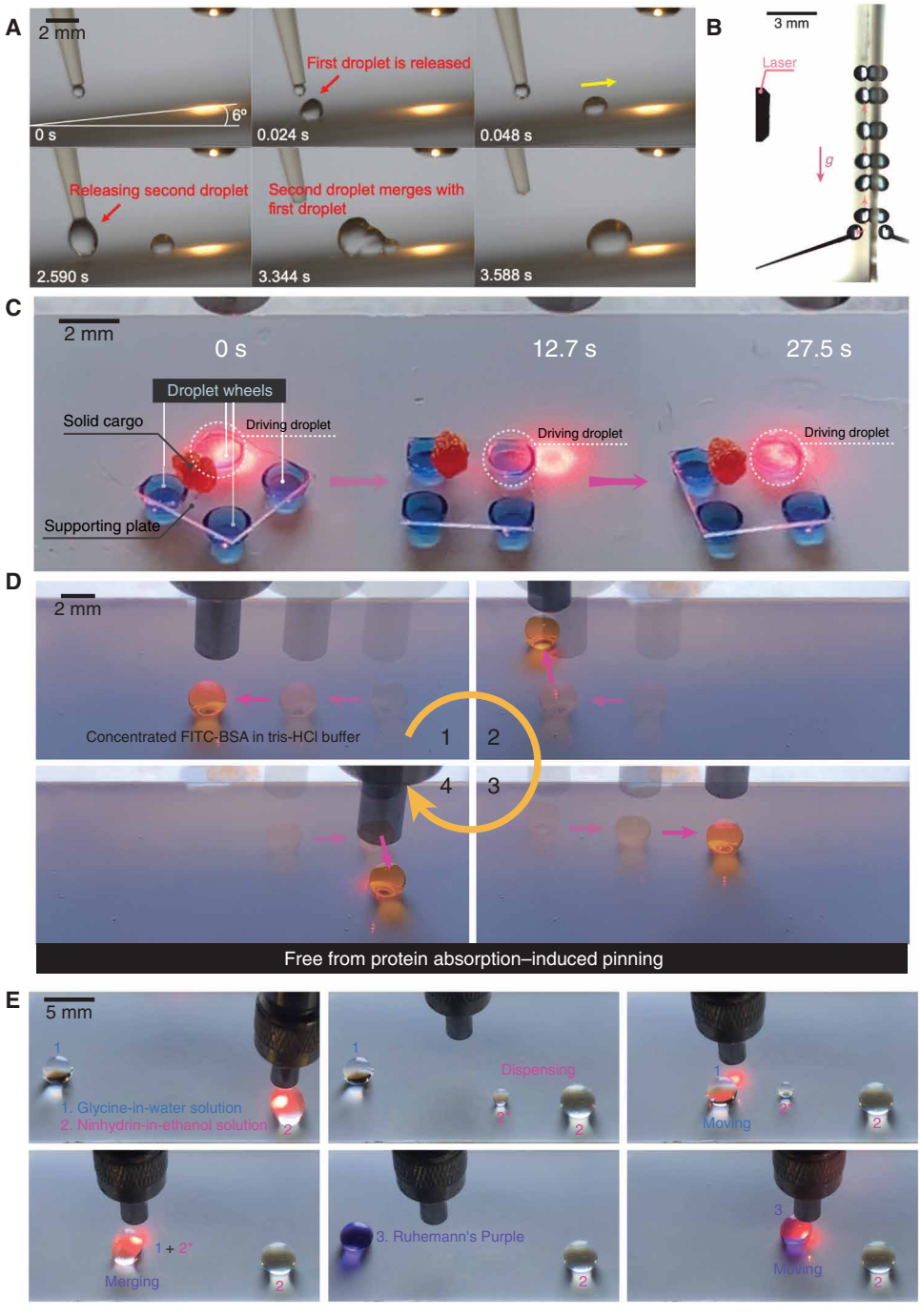

Fig. 5. Versatility and biomolecule compatibility. (**A**) Sequential images showing droplets ascend uphill on the platform tilted at 6°. Laser is turned on at ~−2 s. (**B**) Chronophotograph showing the droplet's climbing of the vertical wall. (**C**) Chronophotograph showing a photo-controlled cargo carrier with four droplet wheels carrying a solid cargo. White dashed circle denotes the driving droplet. (**D**) Chronophotograph showing the lossless manipulation of a 20 mg ml^{-1} FITC-BSA droplet on the photopyroelectric microfluidics platform, enhancing the maximum concentration of deliverable protein by 4000-fold. (**E**) Sequential images showing the detection of glycine using the fundamental fluidic operations on the platform. Photo credit: Wei Li, The University of Hong Kong.

with four liquid wheels can be actively and remotely photo-controlled on the platform. A single beam of light can readily steer, actuate, and brake the carrier. The carrier undergoes guided transport at a velocity as high as 1.0 mm s^{-1}. Such a light-driven cargo carrier can work as robots with soft feet for on-demand transportations of tiny solid objects required in many fields.

Our technique effectively circumvents the long-standing protein absorption challenge encountered in digital microfluidics as well via remarkably upgrading the limit of maximum concentration of deliverable protein by 4000-fold. The high actuation voltages (~100 V) needed in conventional digital microfluidics yield the adsorption of biomolecules onto device surfaces. Such undesired biofouling distorts the assay fidelity and weathers overall performances due to its hindering of the liquids' motions. Without extra additives, the maximum concentration of bovine serum albumin (BSA) in conventional digital microfluidics is, for example, limited to only 0.005 mg ml^{-1} (*31*). Here, we demonstrate that solutions of concentrated fluorescein isothiocyanate (FITC)–BSA (20 mg ml^{-1}) in 10 mM tris-HCl buffer can be easily manipulated on our photopyroelectric microfluidics platform (Fig. 5D and movie S10). The confocal image of the liquid trail (after three cycles of transportation) on our platform probes no detectable protein residue (fig. S8), confirming the practical utility and validity of the platform in biological/chemical processing. The fabrication of such a versatile platform is beautifully simple without any need for microfabrication or electrodes.

Using our photopyroelectric microfluidics platform, we then demonstrate the loss-free detection of amino acid, which involves manipulation of biomolecules (glycine) and low–surface tension liquids (ethanol solutions). As shown in Fig. 5E, a small portion of the probing solution (2% ninhydrin in ethanol) is first dispensed from its reservoir droplet. Then, the analyte droplet (10% glycine in water) is navigated toward the probing one, inducing coalescence and triggering colorimetric reaction (*35*, *36*). The merged droplet gradually turns purple, confirming the existence of amino acid. Thus, our platform can accommodate liquids spanning a wide spectrum of surface tensions, showing its great potential in analytical chemistries, medical diagnosis, and biomedical assays.

DISCUSSION

A unique wavy dielectrophoretic force field is induced in response to the light stimuli by a three-layer surface and enables a full landscape of fluidic manipulations in a well-controlled, loss-free manner: moving, merging, dispensing, and splitting. This force field can be readily modified by superimposing multiple light irradiations for a much richer fluidic operation and droplet patterning. Together with its universality over a wide range of fluid types and volumes, the technique works as a precision wetting-proof liquid tweezer to maneuver fluids on demand, thus being of considerable significance both for biological/chemical fluidic processing where buffers, organic liquids, and even corrosive fluids participate in multistep and repeated reactions, and for fluidic engineering and manufacturing where precision patterning, printing, and building of multicompartment droplets are needed.

MATERIALS AND METHODS

Chemicals

1*H*,1*H*,2*H*,2*H*-perfluorodecyltrichlorosilane (PFDTS) (97%) was purchased from Gelest. Tetraethyl orthosilicate (≥99%), cyclohexane (≥99%), 1,2-dichloroethane (≥99%), *n*-octanol (≥99%), acetic acid (≥99%), toluene (≥99.5%), *n*-decanol (99%), benzyl ether (99%), glycerol (≥99.5%), and FITC-BSA were purchased from Sigma-Aldrich. Tris(hydroxymethyl)aminomethane (>99.0%) was purchased from Tokyo Chemical Industry Corporation. Ammonium hydroxide (28 to 30% in water), hydrochloric acid (37% in water), and DCM (99.6%) were purchased from Acros. Ninhydrin (ACS reagent), glycine (99.5%), Nile red (97.5%), and *N*,*N*-dimethylformamide (99.9%) were purchased from J&K Scientific. Silicone oil (0.65 mPa·s) and Sylgard 184 silicone elastomer kit were purchased from Dow Corning. *n*-Heptane (99%), *n*-octane (>99%), *n*-decane (>99%), *n*-dodecane (>99%), *n*-hexadecane (98%), *n*-butanol (≥99.7%), ethyl acetate (99%), dimethyl carbonate (>98%), and ethylene glycol (>99%) were purchased from Aladdin Industrial Corporation. Dimethyl sulfoxide (>99.98%) was purchased from Thermo Fisher Scientific. Isopropyl alcohol (IPA) (≥99.8%) and acetone (≥99.5%) were purchased from RCI Labscan Limited. Ethanol (absolute) was purchased from VWR International. Deionized water was produced by a deionized water system (DINEC, Hong Kong).

Fabrication of superomniphobic surfaces

The superomniphobic surface was prepared by modifying a previously reported superamphiphobic surface based on candle soot (*25*). The glass slides (Deckglaser glass coverslips and Luoyang Tengjing Glass Co. Ltd.) were first coated with candle soot and then placed in a desiccator together with 1 ml of tetraethoxysilane and 1 ml of ammonia hydroxide. The desiccator was closed, and the vacuum was maintained for 18 hours. Then, the carbon soot core was removed by annealing at 550°C for 3 hours in an oven. The annealed samples were treated with air plasma for 5 min using a plasma cleaner (Harrick, PDC-002-HP) at high power (45 W). Instead of 1*H*,1*H*,2*H*,2*H*-perfluorooctyltrichlorosilane (PFOTS) used in the literature (*25*), the samples were deposited with PFDTS (100 μl) in vacuum for 2 hours to decrease its surface energy. The samples were then super-repellent to ultralow–surface tension oils, such as silicone oil and *n*-heptane, but completely wetted by alcohols like ethanol, IPA, and *n*-butanol because of the strong interaction between alcohols and the unreacted silanol groups on PFDTS. To render the samples superomniphobic, they were then heated at 130°C for 30 min to remove the unreacted PFDTS and promote film restructuring, followed by heat treatment at 310°C for 15 min to promote condensation and lateral cross-linking of silanol groups (*37*, *38*).

Fabrication of photothermal film

Graphene nanoplatelets (6 to 8 nm thick and 5 μm wide; J&K Scientific) were first dispersed in PDMS precursor containing 10 wt % curing agent (Sylgard 184 silicone elastomer kit, Dow Corning) by ultrasonic dispersion. The mixture was then spin coated onto a lithium niobate wafer (z-cut, 0.5 mm thick) at 1000 rpm for 20 s, followed by curing at 50°C for 1 hour.

Contact angle measurement

The measurements of static contact angles, advancing and receding angles, were conducted using a contact angle measuring system (DataPhysics, OCA 25). Contact angle measurements were implemented by advancing and receding a small droplet of liquid (~5 μl) onto the surface using a 1-ml syringe (Hamilton) equipped with a 0.23–mm–outer diameter dosing needle. Fluorocoating agent SFCOAT (AGC Seimi Chemical) was used to render the needle surface to be

omniphobic. The roll-off angles were measured by tilting a stage until the droplet (~5 μl) started to roll off the surface. Averages from at least three independent measurements are used. The surface tensions of the probe liquids were evaluated using a force tensiometer (DataPhysics, DCAT 25) by the Wilhelmy plate method.

Microscopy

The photothermal film and superomniphobic surface were imaged using a Hitachi S4800 scanning electron microscope. Energy-dispersive x-ray scattering was used to obtain the elemental mapping of various elements in photothermal film. The core-shell structure of the superomniphobic surface was observed using a transmission electron microscope (Philips, CM100). The roughness of superomniphobic surface was determined by a laser profilometer (Bruker, ContourGT-K1).

Liquid residue detection

The 10-μl probe liquid [Nile red (1 mg ml^{-1}) in silicone oil] was released to allow rolling or sliding on the tested surfaces (the superomniphobic surface, SLIPs, and PTFE) tilting at 5°. The droplets' traces were observed by fluorescence imaging using an inverted fluorescence microscope (Nikon Eclipse, TS100) equipped with a high-speed camera (Phantom, M110). The fluorescence of Nile red was excited by a 520-nm light source.

Droplet continuous manipulation

To continuously guide the droplet's motion, a 785-nm laser (Shanghai Laser & Optics Century, IRM785RMA-300FC) was fixed on a precise motion control platform (Aerotech, PlanarDL) to control the droplet's moving velocity.

Infrared thermal imaging

The light-triggered thermogenesis of the photothermal film was determined using an infrared thermal camera (Fluke, Ti40).

Transparency

The transparency of the superomniphobic surface was measured using a spectrophotometer (PerkinElmer, Lambda 35) in the 400- to 800-nm range at a scanning rate of 10 nm s^{-1}.

High-speed imaging

High-speed videos were obtained using a Phantom M110 camera.

SUPPLEMENTARY MATERIALS

Supplementary material for this article is available at http://advances.sciencemag.org/cgi/content/full/6/38/eabc1693/DC1

REFERENCES AND NOTES

1. I. Barbulovic-Nad, H. Yang, P. S. Park, A. R. Wheeler, Digital microfluidics for cell-based assays. *Lab Chip* **8**, 519–526 (2008).
2. J. Li, N. S. Ha, T. L. Liu, R. M. van Dam, C.-J. Kim, Ionic-surfactant-mediated electro-dewetting for digital microfluidics. *Nature* **572**, 507–510 (2019).
3. Q. Sun, D. Wang, Y. Li, J. Zhang, S. Ye, J. Cui, L. Chen, Z. Wang, H.-J. Butt, D. Vollmer, X. Deng, Surface charge printing for programmed droplet transport. *Nat. Mater.* **18**, 936–941 (2019).
4. C.-C. Cheng, C. A. Chang, J. A. Yeh, Variable focus dielectric liquid droplet lens. *Opt. Express* **14**, 4101–4106 (2006).
5. N. J. Cira, A. Benusiglio, M. Prakash, Vapour-mediated sensing and motility in two-component droplets. *Nature* **519**, 446–450 (2015).
6. X. Tang, P. Zhu, Y. Tian, X. Zhou, T. Kong, L. Wang, Mechano-regulated surface for manipulating liquid droplets. *Nat. Commun.* **8**, 14831 (2017).
7. Y. Hou, M. Yu, X. Chen, Z. Wang, S. Yao, Recurrent filmwise and dropwise condensation on a beetle mimetic surface. *ACS Nano* **9**, 71–81 (2015).
8. X. Tang, L. Wang, Loss-free photo-manipulation of droplets by pyroelectro-trapping on superhydrophobic surfaces. *ACS Nano* **12**, 8994–9004 (2018).
9. V. Srinivasan, V. K. Pamula, R. B. Fair, An integrated digital microfluidic lab-on-a-chip for clinical diagnostics on human physiological fluids. *Lab Chip* **4**, 310–315 (2004).
10. S. K. Cho, H. Moon, C.-J. Kim, Creating, transporting, cutting, and merging liquid droplets by electrowetting-based actuation for digital microfluidic circuits. *J. Microelectromech. Syst.* **12**, 70–80 (2003).
11. A. Ashkin, Acceleration and trapping of particles by radiation pressure. *Phys. Rev. Lett.* **24**, 156–159 (1970).
12. A. Ashkin, J. M. Dziedzic, J. Bjorkholm, S. Chu, Observation of a single-beam gradient force optical trap for dielectric particles. *Opt. Lett.* **11**, 288–290 (1986).
13. A. Ashkin, J. M. Dziedzic, T. Yamane, Optical trapping and manipulation of single cells using infrared laser beams. *Nature* **330**, 769–771 (1987).
14. A. Ashkin, J. M. Dziedzic, Optical trapping and manipulation of viruses and bacteria. *Science* **235**, 1517–1520 (1987).
15. S.-Y. Park, M. A. Teitell, E. P. Chiou, Single-sided continuous optoelectrowetting (SCOEW) for droplet manipulation with light patterns. *Lab Chip* **10**, 1655–1661 (2010).
16. P. Y. Chiou, H. Moon, H. Toshiyoshi, C.-J. Kim, M. C. Wu, Light actuation of liquid by optoelectrowetting. *Sensors Actuat. A Phys.* **104**, 222–228 (2003).
17. K. Ichimura, S.-K. Oh, M. Nakagawa, Light-driven motion of liquids on a photoresponsive surface. *Science* **288**, 1624–1626 (2000).
18. J. Berná, D. A. Leigh, M. Lubomska, S. M. Mendoza, E. M. Pérez, P. Rudolf, G. Teobaldi, F. Zerbetto, Macroscopic transport by synthetic molecular machines. *Nat. Mater.* **4**, 704–710 (2005).
19. A. Diguet, R.-M. Guillermic, N. Magome, A. Saint-Jalmes, Y. Chen, K. Yoshikawa, D. Baigl, Photomanipulation of a droplet by the chromocapillary effect. *Angew. Chem. Int.* **48**, 9281–9284 (2009).
20. P. Ferraro, S. Coppola, S. Grilli, M. Paturzo, V. Vespini, Dispensing nano–pico droplets and liquid patterning by pyroelectrodynamic shooting. *Nat. Nanotechnol.* **5**, 429–435 (2010).
21. J.-A. Lv, Y. Liu, J. Wei, E. Chen, L. Qin, Y. Yu, Photocontrol of fluid slugs in liquid crystal polymer microactuators. *Nature* **537**, 179–184 (2016).
22. G. Kwon, D. Panchanathan, S. R. Mahmoudi, M. A. Gondal, G. H. McKinley, K. K. Varanasi, Visible light guided manipulation of liquid wettability on photoresponsive surfaces. *Nat. Commun.* **8**, 14968 (2017).
23. J. Won, W. Lee, S. Song, Estimation of the thermocapillary force and its applications to precise droplet control on a microfluidic chip. *Sci. Rep.* **7**, 3062 (2017).
24. J. Wang, W. Gao, H. Zhang, M. Zou, Y. Chen, Y. Zhao, Programmable wettability on photocontrolled graphene film. *Sci. Adv.* **4**, eaat7392 (2018).
25. X. Deng, L. Mammen, H.-J. Butt, D. Vollmer, Candle soot as a template for a transparent robust superamphiphobic coating. *Science* **335**, 67–70 (2012).
26. X. Deng, F. Schellenberger, P. Papadopoulos, D. Vollmer, H.-J. Butt, Liquid drops impacting superamphiphobic coatings. *Langmuir* **29**, 7847–7856 (2013).
27. M. Abdelgawad, A. R. Wheeler, The digital revolution: A new paradigm for microfluidics. *Adv. Mater.* **21**, 920–925 (2009).
28. M. W. Watson, M. Abdelgawad, G. Ye, N. Yonson, J. Trottier, A. R. Wheeler, Microcontact printing-based fabrication of digital microfluidic devices. *Anal. Chem.* **78**, 7877–7885 (2006).
29. S. Pan, R. Guo, M. Björnmalm, J. J. Richardson, L. Li, C. Peng, N. Bertleff-Zieschang, W. Xu, J. Jiang, F. Caruso, Coatings super-repellent to ultralow surface tension liquids. *Nat. Mater.* **17**, 1040–1047 (2018).
30. T.-S. Wong, S. H. Kang, S. K. Y. Tang, E. J. Smythe, B. D. Hatton, A. Grinthal, J. Aizenberg, Bioinspired self-repairing slippery surfaces with pressure-stable omniphobicity. *Nature* **477**, 443–447 (2011).
31. V. N. Luk, G. C. Mo, A. R. Wheeler, Pluronic additives: A solution to sticky problems in digital microfluidics. *Langmuir* **24**, 6382–6389 (2008).
32. C. R. Bowen, J. Taylor, E. LeBoulbar, D. Zabek, A. Chauhan, R. Vaish, Pyroelectric materials and devices for energy harvesting applications. *Energ. Environ. Sci.* **7**, 3836–3856 (2014).
33. T. B. Jones, Dielectrophoretic force calculation. *J. Electrostat.* **6**, 69–82 (1979).
34. M. K. Chaudhury, G. M. Whitesides, How to make water run uphill. *Science* **256**, 1539–1541 (1992).
35. E. W. Yemm, E. C. Cocking, R. E. Ricketts, The determination of amino-acids with ninhydrin. *Analyst* **80**, 209–214 (1955).
36. H. Rosen, A modified ninhydrin colorimetric analysis for amino acids. *Arch. Biochem. Biophys.* **67**, 10–15 (1957).
37. D. Devaprakasam, S. Sampath, S. K. Biswas, Thermal stability of perfluoroalkyl silane self-assembled on a polycrystalline aluminum surface. *Langmuir* **20**, 1329–1334 (2004).
38. B. C. Bunker, R. W. CarPick, R. A. Assink, M. L. Thomas, M. G. Hankins, J. A. Voigt, D. Sipola, M. P. de Boer, G. L. Gulley, The impact of solution agglomeration on the deposition of self-assembled monolayers. *Langmuir* **16**, 7742–7751 (2000).

39. J. Brzoska, F. Brochard-Wyart, F. Rondelez, Motions of droplets on hydrophobic model surfaces induced by thermal gradients. *Langmuir* **9**, 2220–2224 (1993).
40. F. Brochard, Motions of droplets on solid surfaces induced by chemical or thermal gradients. *Langmuir* **5**, 432–438 (1989).
41. M. M. Nahar, J. B. Nikapitiya, S. M. You, H. Moon, Droplet velocity in an electrowetting on dielectric digital microfluidic device. *Micromachines* **7**, 71–86 (2016).
42. C. Dong, T. Chen, J. Gao, Y. Jia, P.-I. Mak, M.-I. Vai, R. P. Martins, On the droplet velocity and electrode lifetime of digital microfluidics: Voltage actuation techniques and comparison. *Microfluid. Nanofluid.* **18**, 673–683 (2015).
43. I. Swyer, R. Fobel, A. R. Wheeler, Velocity saturation in digital microfluidics. *Langmuir* **35**, 5342–5352 (2019).

Acknowledgments: We thank Y. Li, S.-P. Feng, and W.-D. Li for the equipment support, and L. Huang and R. Chen for the valuable discussions. **Funding:** The financial support from the Research Grants Council of Hong Kong (GRF 17204420, 17210319, 17204718, 17237316, and CRF C1018-17G) is acknowledged. This work was also supported, in part, by the Zhejiang Provincial, Hangzhou Municipal, and Lin'an county governments. **Author contributions:** X.T. and L.W. conceived the project. W.L., X.T., and L.W. designed the project. W.L. performed the experiments. W.L., X.T., and L.W. analyzed the data. W.L., X.T., and L.W. wrote the manuscript. L.W. supervised the study. **Competing interests:** The authors declare that they have no competing interests. **Data and materials availability:** All data needed to evaluate the conclusions in the paper are present in the paper and/or the Supplementary Materials. Additional data related to this paper may be requested from the authors.

Submitted 9 April 2020
Accepted 31 July 2020
Published 16 September 2020
10.1126/sciadv.abc1693

Citation: W. Li, X. Tang, L. Wang, Photopyroelectric microfluidics. *Sci. Adv.* **6**, eabc1693 (2020).

Science Advances

Photopyroelectric microfluidics

Wei Li, Xin Tang and Liqiu Wang

Sci Adv **6** (38), eabc1693.
DOI: 10.1126/sciadv.abc1693

Science Advances (ISSN 2375-2548) is published by the American Association for the Advancement of Science, 1200 New York Avenue NW, Washington, DC 20005. The title *Science Advances* is a registered trademark of AAAS.